

Structural phase transition below 250 K in superconducting $\text{K}_{0.75}\text{Fe}_{1.75}\text{Se}_2$

A. Ignatov¹, A. Kumar¹, P. Lubik¹, R. H. Yuan², W. T. Guo², N. L. Wang², K. Rabe¹, and G. Blumberg¹

¹*Department of Physics and Astronomy, Rutgers, The State University of New Jersey, Piscataway, NJ 08854, USA and*

²*Beijing National Laboratory for Condensed Matter Physics,
Institute of Physics, Chinese Academy of Sciences, Beijing 100190, China*

(Dated: September 26, 2012)

Vibrational properties of iron-chalcogenide superconductor $\text{K}_{0.75}\text{Fe}_{1.75}\text{Se}_2$ with $T_c \sim 30$ K have been measured by Raman and optical spectroscopies over temperature range of 3-300 K. Sample undergoes $I4/m \rightarrow I4$ structural phase transition accompanied by loss of inversion symmetry at T_1 , below 250 K, observed as appearance of new fully-symmetric Raman mode at $\sim 165 \text{ cm}^{-1}$. Small vibration mode anomalies are also observed at $T_2 \sim 160$ K. From first-principles vibrational analysis of antiferromagnetic $\text{K}_{0.8}\text{Fe}_{1.6}\text{Se}_2$ utilizing pseudopotentials all observed Raman and infrared modes have been assigned and the displacement patterns of the new Raman mode identified as involving predominantly the Se atoms.

PACS numbers: 78.30.-j, 74.70.Xa, 74.25.Kc

I. INTRODUCTION

Discovery of high- T_c superconductivity in iron-based chalcogenides $\text{A}_y\text{Fe}_{1.6+x}\text{Se}_2$ ($\text{A}=\text{K}, \text{Rb}, \text{Cs}, \text{ and } \text{Tl}$) Ref. [1] raised considerable attention since the materials exhibit unusual physical properties. Parent compound ($y=1, x=0$) is an insulator,^{2,3} crystalizes into $\sqrt{5}x\sqrt{5}x1$ $I4/m$ Fe vacancy-ordering structure, and exhibits antiferromagnetic (AFM) order below a Neél temperature of ~ 560 K Ref.[4]. Doping with alkaline metals or Tl ($y < 1$) apparently preserves the Fe vacancy-ordering and give rise to superconductivity in samples with close to 2:4:5 stoichiometry⁵. Early transport² and neutron diffraction⁴ studies suggested that the superconductivity coexists with AFM order. Alternatively, the doping is discussed in terms of microscopic phase separation⁶⁻¹⁰: a mixture of vacancy-ordered AFM insulating phase and superconducting phase (SC). Due to recent experimental evidences¹¹⁻¹⁴ the consensus seems emerge: the AFM and SC phases are specially separated, the AFM phase occupies from ~ 80 Ref. [11] to 95 % Ref. [12] of the sample volume, and SC phase is homogeneous and does not contains Fe-vacancies nor magnetic moments.¹²⁻¹⁴

Raman scattering study of superconducting $\text{K}_{0.8}\text{Fe}_{1.6}\text{Se}_2$ observed at least 13 phonon modes¹⁵. The crystal symmetry of sample was determined as C_{4h} or lower. Zhang *et al.* performed LDA vibration analysis of nonmagnetic $I4/m$ $\text{K}_{0.8}\text{Fe}_{1.6}\text{Se}_2$ phase and assigned majority of observed Raman modes. The vibrational properties $\text{K}_{0.88}\text{Fe}_{1.63}\text{S}_2$ isostructural to $\text{K}_{0.8}\text{Fe}_{1.6}\text{Se}_2$ confirmed Fe-vacancy ordering: 14 Raman active modes predicted by factor-group analysis were observed and assigned. The authors concluded that the phonon energies in the range of 80-300 K are driven by anharmonicity effects without any signatures of electron-phonon interaction¹⁶. Impact of iron and potassium composition on Raman vibration spectra of $\text{A}_{0.8}\text{Fe}_{1.6}\text{Se}_2$ ($\text{A}=\text{K}, \text{Rb}, \text{ and } \text{Tl}$) was presented in Ref. [17].

The optical studies to date showed at least ten IR-active modes at low temperatures.^{18,19} The in-plane optical conductivity of ($T_c = 31$ K) is incoherent at 300 K, dominated by IR-active modes and high-frequency excitations¹⁹, but become coherent just above the T_c . Small carrier concentration

prompted authors^{10,19} to suggest that the global superconductivity is due to Josephson coupling of nanoscale-sized superconducting phase in the AFM ordered insulating phase.

In this paper we report on Raman scattering and *ab*-plain optical conductivity studies of superconducting $\text{K}_{0.75}\text{Fe}_{1.75}\text{Se}_2$ ($T_c \sim 30$ K) in the T -range from 3 to 300 K. At least 19 Raman-active and 12 IR-active modes are observed at 3 K. The $\sim 136, 143, 242$, and 277 cm^{-1} Raman and $\sim 208 \text{ cm}^{-1}$ IR mode exhibit Fano-like shape. The Raman Fano modes are due the vibration coupling to AFM spin fluctuations, while the IR- mode is coupled to charge carriers in low-frequency part of optical conductivity. Raman phonon linewidth contains approximately equal contributions of two-phonon lattice anharmonicity on one hand and bare self-energy and broadening due to intrinsic defects on the other hand, except for the $\sim 100 \text{ cm}^{-1}$ mode dominated by inhomogeneous broadening. We show that $\text{K}_{0.75}\text{Fe}_{1.75}\text{Se}_2$ undergoes $I4/m \rightarrow I4$ structural phase transition at T_1 below 250 K. Several modes which are not Raman- and IR-active in the measured geometry in $I4/m$ become clearly visible in $I4$ phase. Symmetry of the Se-Fe slab is broken at T_1 . At $T_2 \sim 160$ K Raman vibration modes exhibit weak anomalies seen as small discontinuity of vibration frequencies and change in vibration intensity vs temperature dependencies. Raman vibration intensities of a few modes increases between T_1 and T_2 , saturating above the T_2 , except for three modes dominated by *c*-axis atomic displacements: *c*-axis structural distortions within the slab appear to build up on cooling down to 3 K. The low-frequency optical conductivity displays weak temperature dependence above T_1 followed by faster increase below the T_2 .

II. EXPERIMENTAL

The crystal of iron-chalcogenide superconductors were grown by a self-melting method with nominal concentration of 0.8:2.1:2.0 (K:Fe:Se). The actual chemical composition was determined by EDXS as $\text{K}_{0.75}\text{Fe}_{1.75}\text{Se}_2$ (KFS). Two-step transitions were seen in resistivity curve¹⁰, a sharp drop at 42 K is followed by a major superconducting transition with

$T_c \sim 30$ K. Further details of sample characterization can be found elsewhere.¹⁰

KFS crystals were never exposed to air. Sealed vial was open under 99.999% N_2 , crystal removed and glued on replaceable copper sample holder of a helium Oxford Instruments cryostat, dried and cleaved along the ab -plane, transferred to the He-flow cryostat, and quickly cooled below water freezing temperature. Raman data were obtained on two single crystals. Data presented in this paper refer to the sample with more detail temperature dependence records. It is worth mentioning that results obtained on the second sample are consistent with findings reported here.

Raman spectra were excited with Kr^+ laser line of $\lambda = 647.1$ nm ($E = 1.92$ eV) with less than 10 mW of incident laser power focused into a spot of $\sim 50 \times 100 \mu m^2$ on the freshly cleaved ab -plane crystal surface. The scattered light collected close to the backscattered geometry was focused to a $100 \times 240 \mu m^2$ entrance slits of a custom triple-stage spectrometer equipped with 1800 lines/mm gratings. The instrumental resolution was ~ 1.4 cm^{-1} . To record symmetry resolved Raman spectra we employed circularly polarized light with the optical configurations selecting either the same or opposite chirality for incident and scattered light. The former is referred to as right-right (RR) and the latter as to right-left (RL) configurations. For the C_{4h} point group the B_g (A_g) symmetry is probed in the RL (RR) scattering geometry. Temperature dependent Raman spectra were collected at 3, 45, 100, 150, 160, 180, 200, 260, and 300 K with T -stability better than 0.1 K. An estimated local heating in the laser spot did not exceed 4 K.

Optical measurements were done by Bruker Vertex 80v spectrometer in the frequency range from 25 to 10000 cm^{-1} . The sample was under vacuum of 2×10^{-5} Pa. An in-situ gold and aluminum over-coating technique was used to get the reflectance $R(\omega)$ for light polarized in the KFS (ab)-planes. The real part of conductivity $\sigma_1(\omega)$ was obtained by the Kramers-Kronig transformation of the $R(\omega)$. Optical spectra were collected at 8, 35, 170, and 300 K.

III. RESULTS

$K_{0.8}Fe_{1.6}Se_2$ crystallizes into tetragonal structure $I4/m$ (space group #87) Ref. [4], resulting in the irreducible vibrational representation:

$$\Gamma_{vib} = 9A_g \oplus 8B_g \oplus 8E_g \oplus 9A_u \oplus 7B_u \oplus 10E_u \quad (1)$$

All g -modes are Raman active, but only the A_g and B_g are selected with RR and RL polarizations under the measured geometry. The A_u and E_u vibrations are infrared active along the c -axis and in the ab -plane. The B_u modes are silent. The Fe(1)-vacancy related vibration modes are excluded. Throughout this paper we adopted commonly used site designation: K(1), K(2), Fe(1), Fe(2), Se(1) and Se(2) stand, respectively, for Wyckoff positions of $2a$, $8h$, $4d$, $16i$, $4e$, and $16i$, refer to a legend of Fig.1.

Raman spectra of $K_{0.75}Fe_{1.75}Se_2$ are shown in Fig 1(a) and 1(b) for RL and RR polarizations, respectively. At 300 K,

at least 7(9) modes are observed in RL (RR) in good agreement with $9A_g + 8B_g$ expected in the $I4/m \sqrt{5} \times \sqrt{5}$ cell of $K_{0.8}Fe_{1.6}Se_2$ ¹⁵. The A_g modes at ~ 112 and 267 cm^{-1} are dominated by both chiral and breathing displacements of K(2) and Fe(2) atoms, respectively, Fig. 1(d,e). Below 200 K new modes appear (marked with red arrows): at ~ 201 cm^{-1} in RL and at ~ 165 and ~ 211 cm^{-1} in the RR. The ~ 136 and ~ 277 cm^{-1} phonons in the RL and ~ 144 and ~ 242 cm^{-1} phonons in RR exhibit Fano shapes in whole temperature range of this study. The Fano modes become more symmetric with temperature decrease. Phonon modes parameters are derived from least square fit to experimental data and are summarized in Table I.

Low-frequency region of optical conductivity adopted from Fig. 2 in Ref. [10] is shown in Fig 1(c). In agreement with previous studies^{10,19}, $\sigma_1(\omega)$ is small (characteristic of a poor metal) and it is dominated by the infrared-active vibrations and interband features at higher energies. At 170 and 300 K 9 IR-active modes are observed. The ~ 208 cm^{-1} mode exhibits a Fano-like shape, becoming more asymmetric on cooling. At 170 K and below, at least three new modes (red arrows) are formed, Fig. 1(c). An inspection of the Table I revealed that Raman and IR modes reported in this work do not overlap. It's therefore tempting to conclude that inversion symmetry is preserved. In Section IV we argue that inversion symmetry is actually broken below $T_1 \sim 250$ K. The conductivity displays relatively weak temperature dependence above 170 K followed by about two-fold increase of the continuum as temperature drops from 170 to 35 K. In agreement with previous studies^{18,19}, a Drude-like peak is seen in 35 K data, shortly before sample becomes superconducting.

A. First-principles phonon modes analysis

We performed first-principles density functional theory (DFT) calculations using local density approximation (LDA) with Perdew Zunger (PZ) parameterization for the exchange-correlation energy functional as implemented in *Quantum Espresso* simulation package²⁰. We used ultrasoft pseudopotentials²¹ for K, Fe and norm-conserving pseudopotential²² for Se to describe the interaction between the ionic cores and the valence electrons. The pseudopotentials include 9 valence electrons for K ($3s^2, 3p^6, 4s^2$), 16 for Fe ($3s^2, 3p^6, 3d^6, 4s^2$), and 6 for Se ($4s^2, 4p^4$) atoms. We used a plane wave basis with energy cutoff of 40 Ry for wave function and 360 Ry for the charge density and a $6 \times 6 \times 4$ Monkhorst Pack²³ k -point mesh for the Brillouin zone (BZ) integration.

We optimized structure of $K_{0.8}Fe_{1.6}Se_2$ with a four spin cluster AFM ordering as discussed by Bao *et al.*⁴ using experimental lattice constants obtained at 11 K. The calculation was done using a primitive unit cell of 22 atoms with K(1) and Fe(1) vacancies at $2a$ and $4b$ Wyckoff sites of space group $I4/m$ respectively. Structural optimization is carried through minimization of energy using Hellman-Feynman forces at each atoms in Broyden-Fletcher-Goldfarb-Shanno scheme. The optimized structure shows a very good agree-

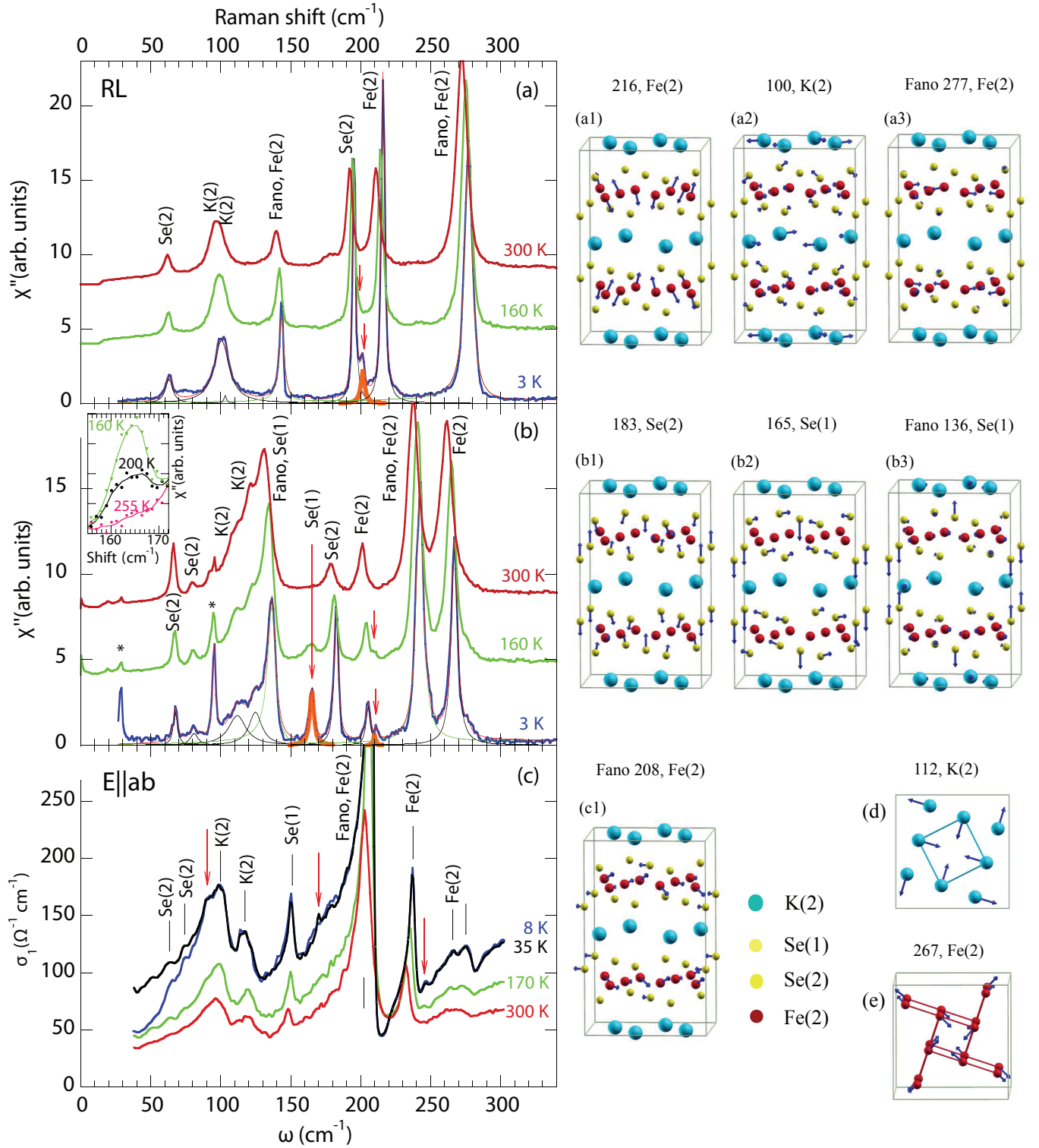


FIG. 1: (Color online) Raman response function of $\text{K}_{0.75}\text{Fe}_{1.75}\text{Se}_2$ in (a) RL and (b) RR channels at 3 (blue), 160 (green), and 300 K (red). (c) ab -plane optical conductivity of $\text{K}_{0.75}\text{Fe}_{1.75}\text{Se}_2$ from the same batch of samples at 8, 35, 170, and 300 K, adopted from Fig. 2 in Ref. [10]. Fits are illustrated on the 3 K spectra. Modes belonging to $I4/m$ Ref. [4] are shown in black (Lorentz) and green (Fano). New phonons appearing at T_1 in the range of 200 to 255 K [insert in (b)], usually referred as seen below ~ 250 K, are shown in orange and marked with arrows. Predominant atomic contribution is labeled for each vibration mode. Computed displacement patterns of selected Raman modes in AFM $I4/m$, $\sqrt{5} \times \sqrt{5}$ unit cells of $\text{K}_{0.8}\text{Fe}_{1.6}\text{Se}_2$ are shown to the right from the vibration spectra: The B_g modes at ~ 216 and 100 cm^{-1} and Fano mode at 277 cm^{-1} are visualized in (a1)-(a3). The displacement patterns of A_g mode at ~ 183 , A_u mode at ~ 165 (becomes Raman active A mode below T_1), and Fano A_g mode at ~ 136 cm^{-1} are shown in (b1), (b2), and (b3). Nine IR-active modes observed throughout the T -range of this study are marked with black bars in (c). At least three new modes (red arrows) seen at 170 K. The displacement patterns for IR Fano mode at ~ 208 cm^{-1} is shown in (c1). 2D atomic displacement patterns of A_g modes involving both chiral and breathing displacements: (d) K(2)-based ~ 112 cm^{-1} and (e) Fe(2) 267 cm^{-1} . All displacements are not up to scale. Two peaks at ~ 29 and 95 cm^{-1} marked by * in (b) are due to plasma lines of Kr- laser.

TABLE I: Assignment of observed Raman and IR vibration modes in $\text{K}_{0.75}\text{Fe}_{1.75}\text{Se}_2$ based on comparison with first-principle calculations utilizing pseudopotentials. Raman and IR modes which appear below $T_1 \sim 250$ K are marked by $^+$ and $^\#$. The Lorentz parameters for Raman and ab -plane IR modes, respectively, at 3 and 35 K were obtained from fit to the experimental data shown in Fig. 1. Here ω_i and Γ_i (in cm^{-1}) are the frequency and FWHM, of the i -th mode. Error bars estimated from covariance are 0.2-0.4 and 0.4-2.0 cm^{-1} for ω_i and Γ_i . Raman data from Ref. [15] and IR data from Ref. [19] are shown for comparison. Computed vibration frequencies are shown for $I4/m$ structure. Total number of modes is less than in Eq(1) because K(1) and acoustic modes are not computed/omitted. Vibration frequencies in $I4$ are less than 10 cm^{-1} apart are not shown in this Table. A_g , B_g , and E_u modes in $I4/m$ becomes, respectively A , B , and E modes in $I4$, refer to Sect IV.

AFM, $I4/m$	Raman (ω, Γ)	Ref.[15]	IR (ω, Γ)	Ref.[19]
63.6 A_g	67.6, 3.5	66.3		
79.9 A_g	81.0, 6.1			
89.0 A_g	111.8, 15.0			
108.2 A_g	124.8, 11.1	123.8		
126.0 A_g	Fano 135.9	134.6		
173.5 A_g	182.5, 3.4			
211.1 A_g	205.3, 3.6	202.9		
236.0 A_g	Fano 242.3	239.4		
265.9 A_g	267.0, 5.3	264.6		
57.9 B_g	63.1, 6.2	61.4		
66.4 B_g	- -			
98.2 B_g	100.6, 12.8	100.6		
117.3 B_g	103.3, 2.1			
134.9 B_g	Fano 143.6	141.7		
206.0 B_g	195.3, 2.6			
224.0 B_g	216.1, 3.0	214.3		
262.7 B_g	Fano 277.1	274.9		
59.0 E_g				
79.9 E_g				
95.1 $E_g^\#$			98.9, 8.2	102.3
104.5 E_g				
156.9 $E_g^\#$			171.2, 4.9	
206.5 E_g				
224.0 E_g				
251.3 $E_g^\#$			246.3, 5.	
61.1 A_u				
92.7 A_u				
96.3 A_u				
172.4 A_u^+	165.2, 3.6			
212.4 A_u^+	211.0, 1.4			
249.7 A_u				
271.0 A_u				
67.7 B_u				
76.0 B_u				
89.3 B_u				
116.2 B_u				
181.9 B_u^+	200.5, 3.4			
240.5 B_u				
273.0 B_u				
62.5 E_u			63.8, 7.1	65.2
73.9 E_u			74.2, 6.1	73.6
85.9 E_u			91.3, 16.	93.7
96.5 E_u			118.5, 10.	121.9
140.7 E_u			150.1, 4.0	151.7
219.3 E_u			Fano 207.6	208.3
233.3 E_u			236.6, 4.4	238.3
268.3 E_u			267.2, 6.1	267.1
			276.1, 4.9	278.6

ment with the experiment. We also allowed inversion symmetry breaking displacement and found that $I4$ structure has slightly lower energy (3.5 meV) compared to $I4/m$, however the splitting of atomic coordinates was very small. We find that both the structures exhibit a band gap of ~ 0.4 eV.

Frequencies of the zone center phonons are determined using linear response method²⁴ for the relaxed structures are listed in the first column of Table I for the AFM $I4/m$ $\text{K}_{0.8}\text{Fe}_{1.6}\text{Se}_2$. Since all nine A_g modes anticipated in the parent AFM $I4/m$ $\text{K}_{0.8}\text{Fe}_{1.6}\text{Se}_2$ are observed at room temperature, there is a unique correspondence between computed and measured vibration frequencies summarized in Table I. Computed B_g mode at 66.4 cm^{-1} is not observed. The B_g vibration at ~ 117.3 cm^{-1} submerges to the broad B_g mode at ~ 100 cm^{-1} , Fig. 1(a) and is revealed in the fit. Importantly, two A_g modes at 79.9 and 89.0 cm^{-1} cannot be reproduced in non-magnetic (NM) $I4/m$ $\sqrt{5}x\sqrt{5}$ structure either undoped $\text{K}_{0.8}\text{Fe}_{1.6}\text{Se}_2$ or vacancy-free KFe_2Se_2 also computed in this work but not listed in the Table I. Therefore, accounting for the spin degree of freedom is essential for accurate mapping of the observed Raman modes. The 8 out of 9 observed IR active modes at 300 K are assigned, Table I and Fig. 1(c). The remaining E_u mode at ~ 278 cm^{-1} is likely due to finite Fe(1) population in the superconducting sample: an extra E_u mode appears in NM vacancy-free $I4/m$ at 294 cm^{-1} . In summary, the observed Raman and IR- vibration frequencies above ~ 200 - 250 K are in good agreement with computed frequencies. Below 200 - 250 K, new Raman modes at ~ 165 , 201, and 211 cm^{-1} and IR-active modes at ~ 99 , 171, and 246 cm^{-1} show up. Their vibration frequencies corresponds well to the computed frequencies of Raman active A, B and IR active E in the $I4$ structure, Table I.

Displacement patterns of selected vibration modes are illustrated in Fig. 1. Raman modes shown in (a1) and (b1) correspond to Fe B_{1g} and As A_{1g} vibrations in the 122 iron-arsenides²⁵. In AFM $I4/m$ both modes got finite (x, y) displacements. The $B_g \sim 100$ cm^{-1} mode is dominated by in-plane K displacements with some admixture of Se and Fe displacements. Its large T -independent linewidth is related to static disorder associated with K(2) sites. The $A_u \sim 172.4$ cm^{-1} patterns are shown in (b2). Being non-Raman active in the AFM $I4/m$ phase it becomes new Raman mode A in the low- T phase AFM $I4$, Fig. 1(b2). Fig. 1 visualizes atomic displacement of one IR-active (c1) and two out of four observed Raman active Fano modes (a3 and b3) discussed in this paper. The striking feature of all but Se-based $A_g \sim 136$ cm^{-1} is essential involvement of Fe(2) atomic displacements. In $\text{K}_{0.8}\text{Fe}_{1.6}\text{Se}_2$ Fe atoms carry magnetic moment as large as $3.3\mu_B$ Ref. [4], while electronic structure near E_f is dominated by Fe d -states³. The Fano modes coupling to electronic and magnetic degrees of freedom are explored in the following section.

B. Origin of Fano vibration modes

Asymmetric line shapes are characteristic of Fano resonances arising from coupling between the phonons and an

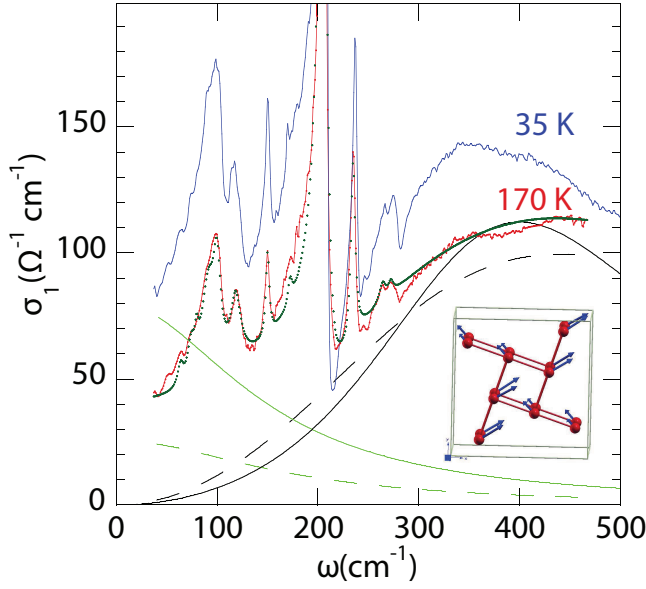


FIG. 2: (Color online) Optical conductivity at 35 K (blue) and 170 K (red) along with a fitting curve (dark green dots). Drude components (green) and MIR Lorentz terms (black) are shown with solid(dashed) curves for 35(170) K. Insert: c-axis view of ab - plane displacement patterns (not up to scale) of the Fe(2) atoms.

electronic continuum, electronic or magnetic in origin. Dipole transition in the IR- absorption does not directly couple the AFM excitations, but couples charge carriers. Raman scattering probes both electronic and magnetic excitations. The 208 cm^{-1} IR- and $\sim 144, 242$, and 277 cm^{-1} Raman Fano modes are dominated by Fe(2) atomic displacements. Interestingly, the IR mode gets more asymmetric [Fig. 2] while four Raman modes [Fig. 3(a-d)] become more symmetric on cooling.

The optical conductivity at 35 and 170 K is shown in Fig. 2. Taking 170 K spectrum as an example, the experimental conductivity is fitted as sum of Drude peak (dashed green), broad Lorentz component (dashed black) describing interband transition at $\sim 400 \text{ cm}^{-1}$, the beginning of mid-infrared (MIR) peak, and eleven Lorentz and one Fano phonon modes. Both Drude and MIR become slightly more coherent and better pronounced as temperature decreases to 35 K. At frequency of Fano mode, the Dude contribution increases, while the MIR contribution slightly decreases. Therefore, enhancement in the IR Fano peak asymmetry is due to the vibration coupling to charge carriers in the Drude tail.

Four Fano Raman modes are presented in Fig. 3(a)-(d) at 3 and 160 K. They were obtained by removal of fitted in phonons from data shown in Fig 1(a,b). Clearly, all Raman modes exhibit similar T dependence: (a) they are less symmetric, and (b) they characterized by larger background at 160 K than at 3 K. The observed behavior is reminiscent of T -dependence of a new mode observed in AFM 122 systems. The mode appears at T_N as a Fano-shaped one and it becomes progressively more symmetric with temperature decrease. The Fano peak derives from vibration coupling to

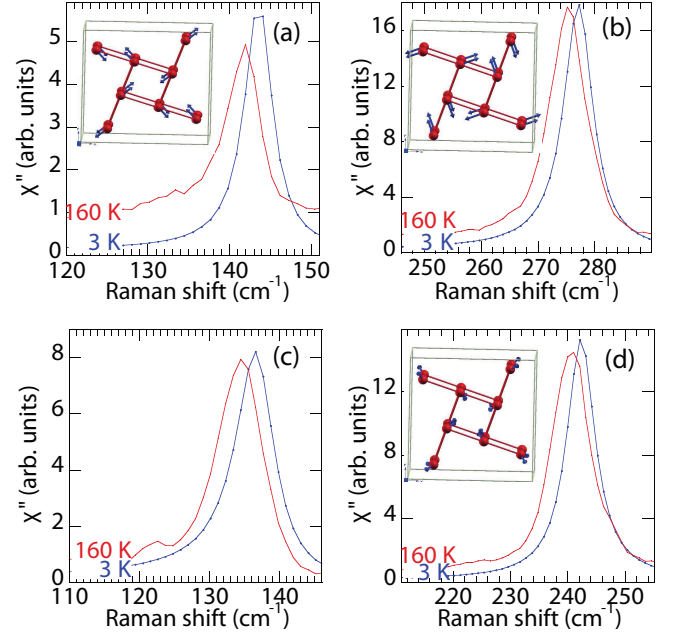


FIG. 3: (Color online) Raman Fano modes for (a) ~ 142 and (b) $\sim 277 \text{ cm}^{-1}$ in RL and (c) ~ 137 and (d) $\sim 242 \text{ cm}^{-1}$ in RR. Inserts: c-axis view of ab - plane displacement patterns (not up to scale) of the Fe(2) atoms. The 3D displacement patterns are shown in Fig. 1.

magnetic continuum, the AFM spin fluctuations.

C. Temperature dependence of Raman mode linewidth and phonon frequencies

Selected linewidth and phonon frequencies as function of temperature are shown in Fig. 4. The T -dependent phonon frequencies qualitatively agree with those reported by Zhang *et al* in $\text{K}_{0.8}\text{Fe}_{1.6}\text{Se}_2$ (Fig 5 in Ref. [15]) and by Lazarević *et al* in isostructural $\text{K}_{0.88}\text{Fe}_{1.63}\text{S}_2$ (Fig. 3(b-j) in Ref. [16]). In the latter work, the authors concluded that the Raman active phonon energies in the range of 80-300 K are fully driven by anharmonicity effects¹⁶. Interpretation offered in the present work is different: the residual linewidth is compatible [Fig. 4(a,c)] or larger [Fig. 4(e)] than the temperature dependent increment between 3 and 300 K. Therefore, self-energy of non-Fano phonons (i.e. at ~ 195 and 216 cm^{-1} in B_g and at $\sim 68, 205$, and 267 cm^{-1} in A_g channels) consist of approximately equal contributions of two-phonon lattice anharmonicity on one hand and bare self-energy and broadening due to intrinsic defects on the other. Self-energy of $\sim 100 \text{ cm}^{-1}$ mode involving the K(2) atomic displacements is dominated by inhomogeneous broadening. The new $\sim 165 \text{ cm}^{-1}$ mode appearing at T_1 in the range of 200 to 250 K becomes fully coherent below ~ 40 -60 K: the linewidth presented in Fig. 4(g) quickly reduces by ~ 5 times as temperature decreases from 200 to 60 K, followed by saturation below ~ 40 K. The mode hardens on cooling by $\sim 1.0 \text{ cm}^{-1}$ [Fig. 4(h)] in the traceable T -range.

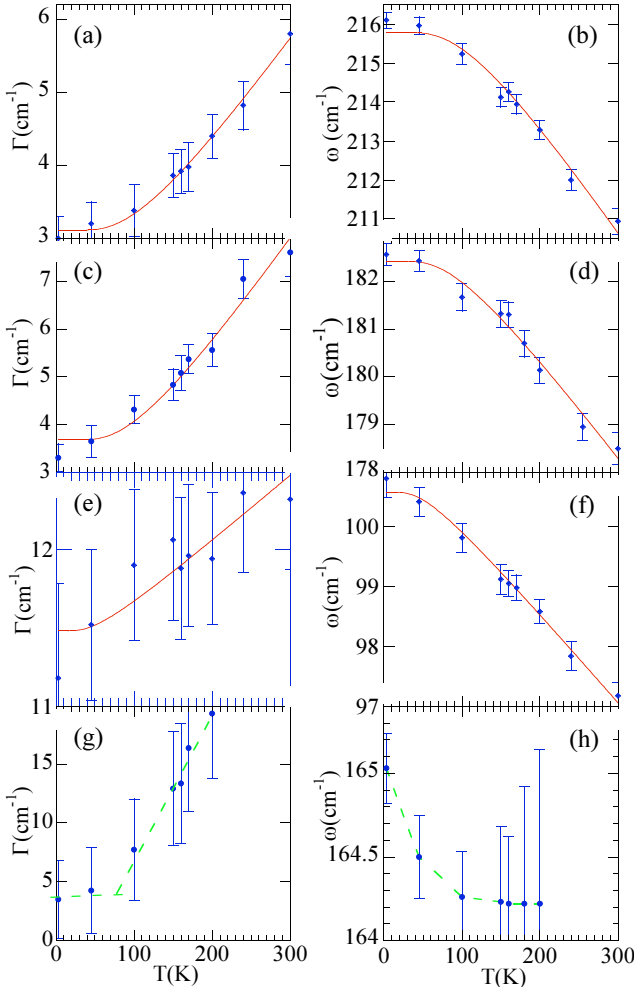


FIG. 4: (Color online) Linewidth (first row) and subsequent phonon frequencies (second row) of Fe(2) $B_g \sim 216$, Se(2) $A_g \sim 182$, K(2) $B_g \sim 100$, and Se(1) $A_g \sim 165 \text{ cm}^{-1}$ modes. Solid red lines describe two-phonon anharmonic decay²⁶. Dashed green lines are guided to the eye. The atomic displacement patterns of the modes are visualized in Fig 1 (a1, b1, a2, and b2).

IV. DISCUSSION

The new 165 cm^{-1} mode appearing at T_1 in the range of 200-250 K, [insert of Fig. 1(b)], usually referred as seen at T_1 below $\sim 250 \text{ K}$ throughout this paper, is not Raman active in the $I4/m$ phase (Table I), fully symmetric in character, and it quickly becomes coherent with T -decrease [Fig. 3(g)]. The question arises whether this mode signifies crystal symmetry lowering on a structural phase transition. If it is associated with symmetry lowering, it would become allowed phonon mode in one of subgroups of C_{4h} . The C_{4h} encompass the C_4 (loss of inversion and rotation-reflection), C_{2h} (loss of 4^{th} order rotation axis), S_4 (loss of inversion and 4^{th} order rotation axis), C_2 (loss of inversion, 4^{th} order rotation axis, and rotation-reflection), and C_1 (primitive) subgroups. We did not observe leaking of four-fold axis symmetry that would results in the cross-polarization intensity leakages beyond small leak-

ages of polarization optics which don't correlate with temperature dependence of the 165 cm^{-1} mode. Thus, C_{2h} , C_2 , and C_1 subgroups are excluded. The S_4 (space group #82) is excluded because there is no new A -type Se(1) mode associated with the transition. Therefore, $I4/m$ (C_{4h} , space group #87) becomes $I4$ (C_4 , space group #79). From the factor-group analysis A_g , B_g , and E_u modes in C_{4h} becomes, respectively A , B , and E modes in C_4 . Instead of $9A_g + 8B_g$ Raman active and $8E_u$ infrared active modes in high- T $I4m$ phase one would expect to encounter $17A + 15B$ Raman and $17E$ IR-active modes in low- T phase under the measured geometry. Here we excluded acoustic and Fe(1)-related modes, since the Fe(1)-site is mostly empty site in $\text{K}_{0.75}\text{Fe}_{1.75}\text{Se}_2$. The Raman active modes do not overlap with ab -plane IR active modes, not only in high- but in low- T phases. This explains seemingly puzzling absence of IR mode leakages into the Raman spectra noted in Section 3. Since new Raman modes (at ~ 165 , 201 , and 211 cm^{-1} and IR-active modes (at ~ 99 , 171 , and 246 cm^{-1}) appears below T_1 and those modes are non-Raman(non-IR) active $A_u(E_g)$ or silent B_u in $I4m$ (Table I) we suggest that $\text{K}_{0.75}\text{Fe}_{1.75}\text{Se}_2$ undergoes $I4/m \rightarrow I4$ structural phase transition accompanied by loss of inversion symmetry at T_1 below $\sim 250 \text{ K}$. Our first-principles calculations utilizing pseudopotentials also narrowly favor $I4$ over the $I4/m$ structure. The small total energy difference is likely because computations do not include all correlations and/or the calculations are performed for the undoped $\text{K}_{0.8}\text{Fe}_{1.6}\text{Se}_2$.

Temperature dependence of selected phonon frequencies and intensities are shown in Fig. 5(a,b) and 5(c,d), respectively. Apart from the structural phase transition at T_1 below $\sim 250 \text{ K}$, clearly there is a second characteristic temperature, $T_2 \sim 160 \text{ K}$. At T_2 majority of phonon vibration frequencies exhibit consistent discontinuity up to $\sim 0.3 \text{ cm}^{-1}$ [Fig. 5(a, b)], while quite a few modes display slop changes in their intensity vs temperature dependencies [Fig. 5(c, d)]. Since no new vibration modes (Raman or IR) are observed below the T_2 the T_2 is not constituent a structural phase transition, but rather referred as phonon anomaly temperature. Anomaly of a single A_g mode at 66 cm^{-1} at 160 K was mentioned by Zhang *et al.*¹⁵. We would like to point out that the phonon anomalies seen at the $T_2 \sim 160 \text{ K}$ involve majority of measured Raman modes.

From experimental data at hand we could point out two implications of the observed structural phase transition on low- T properties of $\text{K}_{0.75}\text{Fe}_{1.75}\text{Se}_2$. First, symmetry of the Se(1,2)-Fe(2) slab is broken at T_1 , sample becomes ferroelectric, and c -axis structural distortions within the stab appears to build up on cooling. This is seen in Raman phonon peak intensities, Fig. 5(c,d), which are directly proportional to polarizability tensor. As sample enters the low- T phase ($T < T_1$), polarizability of quite a few Raman-active modes build-up till $\sim T_2$, followed by saturation at $T < T_2$ (B -symmetry at 63 , 100.6 , and 277 ; A -symmetry at 81 and 267 , Fano-shape 136 and 242 cm^{-1}) or reduction (A -symmetry at 68 , 112 , and 125 cm^{-1}). However, polarizabilities of Fe(2)-based B mode at ~ 216 , As(2)-based A mode at ~ 183 , and As(1)-based A mode at $\sim 165 \text{ cm}^{-1}$ continue to build up till ~ 45 , 3 , and 3 K , respectively. The scaling relationships among the three

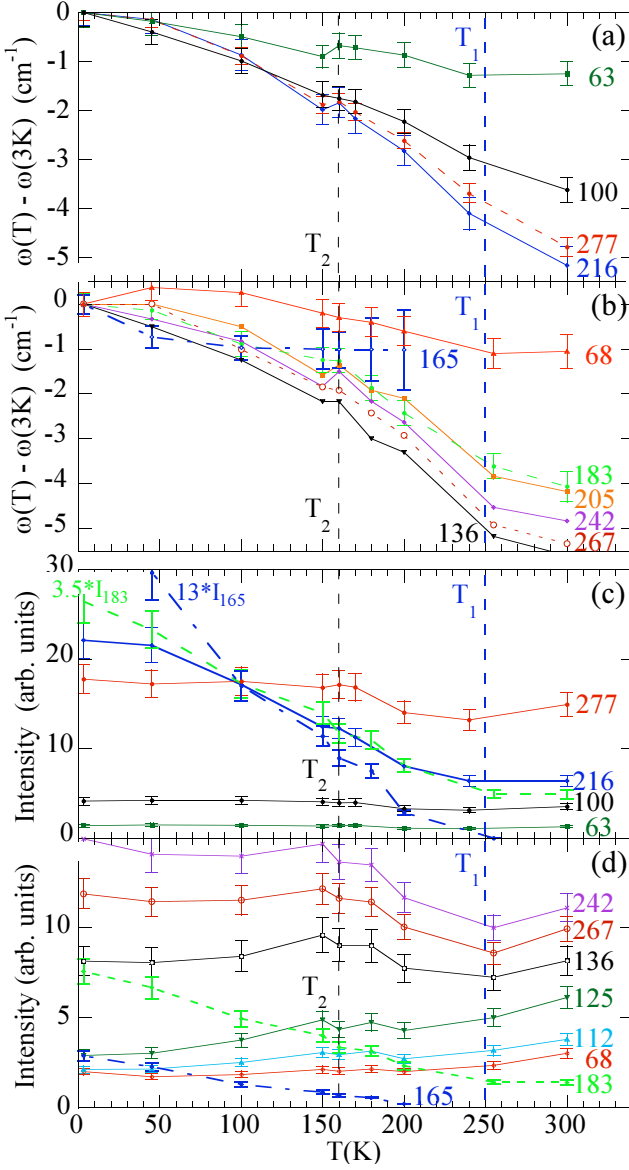


FIG. 5: (Color online) Temperature dependence of selected phonon frequencies (a,b) and intensities (c,d). Some error bars are omitted in (b) for clarity. T_1 and T_2 mark temperatures of structural phase transition at ~ 250 K and phonon anomalies at ~ 160 K. In (c) intensity of the Fe(2)-based $B(B_g) \sim 216$ cm^{-1} (solid blue line) scales almost perfectly to 3.5 ± 0.2 times intensity of Se(2)-based $A(A_g) \sim 183$ cm^{-1} (dashed green line) in the range of 45 to 250 K. It also satisfactory scales to 13 ± 1 times intensity of the Se(1)-based $A \sim 165$ cm^{-1} (dot-dashed blue line) in the range of ~ 100 to 200 K. Note there are four Se(2) per one Se(1) atom.

are shown in Fig. 5(c). The scaling is not surprising, giving to similar displacements patterns of the modes along the c -axis [Fig.1(a1), (b1), and (b2)], so that their Raman activities are driven by polarizability of the electronic orbitals forming the Fe-Se slabs. In iron-arsenides (122-systems) the Fe-As slab is perfectly symmetric and the Raman-active As-based A_{1g} mode has extremely low intensity (polarizability) if measured in the same geometry²⁵. It becomes visible upon doping de-

stroying the symmetry of the slab. In $\text{K}_{0.75}\text{Fe}_{1.75}\text{Se}_2$, intrinsic population of Fe- and K- vacancies makes the Se(2)-based $A_g \sim 183$ cm^{-1} mode effortlessly visible at room temperature. The atomic displacements associated with the $I4/m \rightarrow I4$ phase transition which have sizable ab -plane components are likely quenched below T_2 , while c -axis displacements continue to build up on cooling. Second implication concerns the temperature dependence of low-frequency optical conductivity shown in Fig. 1(c). The conductivity displays weak temperature dependence above T_1 followed by faster increase below the T_2 , in agreement with similar temperature dependence reported by Homes *et al.*¹⁹

Onset of superconductivity at ~ 30 K has little effect on phonons. Using 3 and 45 K data points, the upper estimated phonon energy shifts are -0.3 ± 0.4 cm^{-1} ($|\Delta\omega|/\omega \sim 0.44\%$) for 67.6 cm^{-1} and $+0.6 \pm 0.4$ cm^{-1} ($|\Delta\omega|/\omega \sim 0.36\%$) for 165.0 cm^{-1} modes. Small frequencies renormalization implies either weak e - ph interaction or that the phonons used in our analysis belongs to the AFM phase in the phase separated models^{6,7,10,12,13}: spectator AFM phonons would not feel onset of the superconductivity, unless via the proximity effect.

V. CONCLUSIONS

Raman scattering and optical conductivity were used to determine lattice vibration frequencies of superconducting crystal $\text{K}_{0.75}\text{Fe}_{1.75}\text{Se}_2$ in temperature range from 3 to 300 K. 19 Raman-active and 12 IR-active modes are observed at 3 K. The ~ 136 , 143, 242, and 277 cm^{-1} Raman and ~ 208 cm^{-1} IR mode exhibit Fano-like shape. The Raman Fano modes are due to the vibration coupling to AFM spin fluctuations, while the IR- mode is coupled to charge carriers in low-frequency part of optical conductivity. Raman phonon linewidths contain approximately equal contributions of two-phonon lattice anharmonicity on one hand and bare self-energy and broadening due to intrinsic defects on the other hand. The $\text{K}_{0.75}\text{Fe}_{1.75}\text{Se}_2$ undergoes $I4/m$ (space group #87) $\rightarrow I4$ (space group #79) structural phase transition at T_1 below ~ 250 K. Several modes which are not Raman- and IR-active in the measured geometry in $I4/m$ become visible in $I4$ phase including Raman modes at ~ 165 , 201, and 211 cm^{-1} and IR-active modes at ~ 99 , 171, and 246 cm^{-1} . Weak phonon anomalies are also observed at $T_2 \sim 160$ K. Symmetry of the Se(1,2)-Fe(2) slab is broken at T_1 . ab -plane structural distortions are likely quenched below T_2 , while c -axis structural distortions within the slab continues to build up on cooling down to 3 K.

VI. ACKNOWLEDGMENTS

Research at Rutgers was supported by the U.S. DOE, office of BES, Division of Materials Science and Engineering under award de-sc0005463. Research at Beijing National Laboratory for Condensed Matter Physics was supported by the NSFC and 973 projects of MOST (Grant No. 2011CB921701, 2012CB821403).

- ¹ J. Guo, S. Jin, G. Wang, S. Wang, K. Zhu, T. Zhou, M. He, and X. Chen, *Phys. Rev. B* **82**, 180520(R) (2010); A. F. Wang, J. J. Ying, Y. J. Yan, R. H. Liu, X. G. Luo, Z. Y. Li, X. F. Wang, M. Zhang, G. J. Ye, P. Cheng, Z. J. Xiang, and X. H. Chen, *ibid.* **83**, 060512(R) (2011).
- ² R. H. Liu, X. G. Luo, M. Zhang, A. F. Wang, J. J. Ying, X. F. Wang, Y. J. Yan, Z. J. Xiang, P. Cheng, G. J. Ye, Z. Y. Li, and X. H. Chen, *Europhys. Lett.* **94**, 27008 (2011).
- ³ X.-W. Yan, M. Gao, Z.-Y. Lu, and T. Xiang, *Phys. Rev. B* **83**, 233205 (2011).
- ⁴ W. Bao, Q.-Z. Huang, G.-F. Chen, M. A. Green, D.-M. Wang, J.-B. He, and Y.-M. Qiu, *Chin. Phys. Lett.* **28**, 086104 (2011).
- ⁵ Y. J. Yan, M. Zhang, A. F. Wang, J. J. Ying, Z. Y. Li, W. Qin, X. G. Luo, J. Q. Li, J. Hu, and X. H. Chen, *Sci. Rep.* **2**, 212 (2012).
- ⁶ Z. Wang, Y. J. Song, H. L. Shi, Z. W. Wang, Z. Chen, H. F. Tian, G. F. Chen, J. G. Guo, H. X. Yang, and J. Q. Li, *Phys. Rev. B* **83**, 140505 (2011).
- ⁷ A. Ricci, N. Poccia, G. Campi, B. Joseph, G. Arrighetti, L. Barba, M. Reynolds, M. Burghammer, H. Takeya, Y. Mizuguchi, Y. Takano, M. Colapietro, N. L. Saini, and A. Bianconi, *Phys. Rev. B* **84**, 060511 (2011).
- ⁸ Jun Zhao, Huibo Cao, E. Bourret-Courchesne, D. -H. Lee, and R. J. Birgeneau, *arXiv:1205.5992*.
- ⁹ D. A. Torchetti, M. Fu, D. C. Christensen, K. J. Nelson, T. Imai, H. C. Lei, and C. Petrovic, *Phys. Rev. B* **83**, 104508 (2011).
- ¹⁰ R. H. Yuan, T. Dong, Y. J. Song, P. Zheng, G. F. Chen, J. P. Hu, J. Q. Li, and N. L. Wang, *Sci. Rep.* **2**, 221 (2012).
- ¹¹ A. Charnukha, A. Cvitkovic, T. Prokscha, D. Pröpper, N. Ocelic, A. Suter, Z. Salman, E. Morenzoni, J. Deisenhofer, V. Tsurkan, A. Loidl, B. Keimer, and A. V. Boris, *Phys. Rev. Lett.* **109**, 017003 (2012).
- ¹² Y. Texier, J. Deisenhofer, V. Tsurkan, A. Loidl, D. S. Inosov, G. Friemel, J. Bobroff, *arXiv:1203.1834*.
- ¹³ G. Friemel, J. T. Park, T. A. Maier, V. Tsurkan, Yuan Li, J. Deisenhofer, H.-A. Krug von Nidda, A. Loidl, A. Ivanov, B. Keimer, and D. S. Inosov, *Phys. Rev. B* **85**, 140511(R) (2012).
- ¹⁴ Wei Li, Hao Ding, Peng Deng, Kai Chang, Canli Song, Ke He, Lili Wang, Xucun Ma, Jiang-Ping Hu, Xi Chen¹, and Qi-Kun Xue, *Nature Physics* **8**, 126 (2012).
- ¹⁵ A. M. Zhang, K. Liu, J. H. Xiao, J. B. He, D. M. Wang, G. F. Chen, B. Normand, and Q. M. Zhang, *Phys. Rev. B* **85**, 024518 (2012).
- ¹⁶ N. Lazarević, Hechang Lei, C. Petrovic, and Z. V. Popović, *Phys. Rev. B* **84**, 214305 (2011).
- ¹⁷ A. M. Zhang, K. Liu, J. H. Xiao, J. B. He, D. M. Wang, G. F. Chen, B. Normand, and Q. M. Zhang, *arXiv:1105.1198*.
- ¹⁸ Z. G. Chen, R. H. Yuan, T. Dong, G. Xu, Y. G. Shi, P. Zheng, J. L. Luo, J. G. Guo, X. L. Chen, and N. L. Wang, *Phys. Rev. B* **83**, 220507(R) (2011).
- ¹⁹ C. C. Homes, Z. J. Xu, J. S. Wen, and G. D. Gu, *Phys. Rev. B* **85**, 180510(R) (2012).
- ²⁰ S. Baroni, A. Dal Corso, S. de Gironcoli, and P. Giannozzi, 2001, <http://www.pwscf.org>.
- ²¹ D. Vanderbilt, *Phys. Rev. B* **41**, 7892(1990).
- ²² D. R. Hamann, M. Schlüter, and C. Chiang, *Phys. Rev. Lett.* **43**, 1494 (1979).
- ²³ H. J. Monkhorst and J. D. Pack, *Phys. Rev. B* **13**, 5188 (1976); H. J. Monkhorst and J. D. Pack, *ibid.* **16**, 1748 (1977).
- ²⁴ S. Baroni, S. de Gironcoli, A. Dal Corso, and P. Giannozzi, *Rev. Mod. Phys.* **73**, 515 (2001).
- ²⁵ A. P. Litvinchuk, V. G. Hadjiev, M. N. Iliev, Bing Lv, A. M. Guloy, and C. W. Chu, *Phys. Rev. B* **78**, 060503(R) (2008).
- ²⁶ M. Balkanski, R. F. Wallis, and E. Haro, *Phys. Rev. B* **28**, 1928 (1983).